Materials LAB

RESEARCH ARTICLE

Materials Lab 2025, 4, 250006

In-situ surface vanadate anchoring strategy for robust and efficient seawater oxidation

Jooheon Sun[1], Jiseok Kwon[1], Seunggun Choi[1], Yeseung Lee[1], Ungyu Paik[1*] and Taeseup Song[1*]

Direct seawater electrolysis is a promising alternative for carbon-neutral energy systems since large-scale hydrogen production is limited by the cost and scarcity of ultrapure water. Yet the high concentration of Cl^- in seawater critically undermines electrocatalyst stability. Herein, we report a novel vanadate-anchoring strategy that simultaneously boosts the activity and durability of $Ni(OH)_2$ anode for alkaline seawater oxidation. Electrochemical anchoring of vanadate onto the $Ni(OH)_2$ surface enables facile surface reconstruction, which significantly modulates the electronic structure of the electrocatalyst and adsorption ability. The tailored electronic structure induced by the anchoring of vanadate steers the reaction along a lattice oxygen-mediated mechanism (LOM). Furthermore, anchored vanadate endows with electrostatic repulsion toward Cl^-, granting durability for direct seawater electrolysis. The optimized vanadate-anchored electrocatalyst, $Ni(OH)_2$-Vi, requires only 284 mV at 10 mA cm^{-2} in simulated alkaline seawater, surpassing 328 mV of $Ni(OH)_2$ and 314 mV of $Ni(OH)_2$-Pi. Also during a 200 h chronopotentiometry at 100 mA cm^{-2}, $Ni(OH)_2$-Vi shows a degradation rate of only 0.198 mV h^{-1}, markedly lower than the 0.812 mV h^{-1} for $Ni(OH)_2$ and 0.780 mV h^{-1} for $Ni(OH)_2$-Pi.

The demand for hydrogen is rapidly increasing as the world aims for carbon neutrality. Water electrolysis is recognized as a key technology for hydrogen production.[1–4] Currently, the most technologically advanced methods of water electrolysis are alkaline water electrolysis (AWE) and proton exchange membrane water electrolysis (PEMWE).[5–8] Both methods require a water purification process, which adds to operational costs.[9] Additionally, the high-purity water necessary for conventional AWE and PEMWE is already in demand for various uses, including agriculture, raising concerns about resource scarcity.[10] As an alternative, seawater electrolysis is highly attractive because it utilizes an abundant resource and offers strong economic viability, especially when integrated with offshore renewable energy power plants.[11]

However, the high concentration of chloride (Cl^-) ions in seawater (~0.5M) significantly reduces the stability of the anode catalyst, which attracts anions electrically, in contrast to pure water electrolysis. ClOR (Chlorine Oxidation Reaction), which competes with OER (Oxygen Evolution Reaction) at the anode, generates chlorine gas (Cl_2) or hypochlorite ions (ClO^-).[12–14] These corrosive chlorine species not only deteriorate the stability of the anode catalyst but also reduce the selectivity of the OER. Notably, in a seawater electrolysis system, the equilibrium potential difference between ClOR and OER is substantially greater in an alkaline electrolyte (~480 mV) than in an acidic or neutral electrolyte (a minimum of ~180 mV).[15] While electrolysis under alkaline conditions can thus thermodynamically avoid ClOR, the two-electron accompanied ClOR can still kinetically overshadow the four-electron accompanied OER, which has sluggish kinetics.[16] Furthermore, the strong adsorption strength of chloride on the catalyst continuously drives an aggressive attack on the metal substrate, ultimately leading to its corrosive failure.[17] Consequently, for efficient seawater oxidation, it is essential to develop catalysts that exhibit high activity and fundamentally block chloride to ensure high stability.

One of the most interesting strategies for improving the stability of seawater oxidation catalysts is the electrostatic repulsion of chloride by incorporating an oxyanion into their surface structure.[18–20] The oxyanion not only plays a role in the catalyst reconstruction process, facilitating the formation of the real active phase known as amorphous metal oxyhydroxide (MOOH), but it also enhances the intrinsic activity of MOOH.[21–24] Furthermore, the negative charge of the oxyanion effectively helps repel chloride, allowing electrocatalysts that contain oxyanions to serve as optimal catalysts for seawater oxidation. Luo et al. developed a sulfur-doped cobalt-nickel bimetallic phosphide (CoNiPS) that transforms in situ into an oxyanion-decorated Co(Ni)OOH (referred to as R-CoNiPS) catalyst under operating conditions.[23] The formation of phosphate (PO_4^{3-}) and sulfate (SO_4^{2-}) enhances the oxygen evolution reaction (OER) by regulating and stabilizing the active Co(Ni)OOH species while simultaneously blocking chloride adsorption to enhance anti-corrosion ability. Li et al. also fabricated a nanoarray electrode in which Ni_3Fe-LDH nanosheets were grown on CoP_x nanowires.[25] The catalyst formed a surface-anchored phosphate layer while activating, which act as good proton acceptors, accelerating water disso-

[1] *Department of Energy Engineering, 222 Wangsimni-ro, Seongdong-gu, Hanyang University, Seoul 04763, Republic of Korea*

* Corresponding author, E-mail: upaik@hanyang.ac.kr; tssong@hanyang.ac.kr

Received 30 April 2025; Accepted 3 July 2025; Published online 10 July 2025

DOI: 10.54227/mlab.20250006

ciation step and thereby promoting OH^- adsorption to boost OER activity under neutral seawater condition. Beyond facilitating OH^- adsorption, the phosphate overlayer also electrostatically repels chloride ions, mitigating chloride-induced corrosion.

Herein, we introduce the catalyst surface vanadate anchoring strategy for seawater oxidation. Vanadate (VO_4^{3-}) incorporated into the alkaline electrolyte (1M KOH + x M Na_3VO_4) become anchored onto the surface of the reconstructed MOOH phase during electrochemical activation. The anchored vanadate accelerates the surface reconstruction during the activation process, promoting the formation of the highly active NiOOH phase. The vanadate-anchored $Ni(OH)_2$ shows a strong inhibitory effect of tetramethylammonium (TMA^+), which indicates that vanadate steers the reaction away from the water oxidation catalyst's traditional rate-determining OOH-formation step and toward a lattice oxygen-mediated mechanism (LOM). Furthermore, deuteric kinetic-isotope measurements verify the accelerated water deprotonation step, confirming that vanadate directly facilitates the LOM pathway. By optimizing the concentration of vanadate in electrolyte, the $Ni(OH)_2$-Vi exhibits a chloride-blocking ability stronger than the widely adopted phosphate anchoring strategy, achieving overpotentials of 284 mV at 10 mA cm^{-2} in simulated alkaline seawater (1 M KOH + 0.5 M NaCl), compared to 328 mV for pristine $Ni(OH)_2$ and 314 mV for $Ni(OH)_2$-Pi. In addition, $Ni(OH)_2$-Vi shows a degradation rate of only 0.198 mV h^{-1} during a 200 h chronopotentiometry test at 100 mA cm^{-2} in simulated alkaline seawater, whereas $Ni(OH)_2$ and $Ni(OH)_2$-Pi shows 0.812 mV h^{-1} and 0.780 mV h^{-1}, respectively.

Result & Discussion

Material Characterization

The vanadate (VO_4^{3-}) oxyanion was selected as a functional component for water electrolysis based on the following considerations: i) Vanadate exhibits strong electrostatic repulsion toward chloride ions (Cl^-) due to its high negative charge density and stable tetrahedral geometry. ii) The vanadium center in VO_4^{3-} exists in a +5-valence state with empty 3d orbitals, allowing it to act as a strong electron-withdrawing unit to modulate the electronic structure of active center.[26] iii) Compared to $(PO_4)^{3-}$ ligand, $(VO_4)^{3-}$ ligand can act as an active site, showing synergistic interaction with active center.[27,28] Fig. 1a illustrates the synthesis process of a vanadate-anchored $Ni(OH)_2$ (denoted as $Ni(OH)_2$-Vi). It commences with the formation of a $Ni(OH)_2$ pre-catalyst via a simple hydrothermal method. Subsequently, $Ni(OH)_2$-Vi is fabricated by cyclic voltametric electrochemical activation within the 1.0 ~ 1.8 V_{RHE} potential range in 1M KOH electrolyte containing varying molar concentrations of Na_3VO_4. The resulting electrocatalyst comprises a nanosheet array supported on a nickel foam substrate (Fig. 1b-c). The morphology of $Ni(OH)_2$-Vi is identical to that of the electrocatalyst activated in a vanadate-free electrolyte, implying that surface vanadate anchoring does not induce any significant morphological change (Fig. S1). Fig. 1c presents the X-ray diffraction (XRD) pattern of $Ni(OH)_2$-Vi shows $Ni(OH)_2$-Vi remains $Ni(OH)_2$ crystal structure (PDF # 38-0715), confirming that the vanadate anchoring does not significantly alter the crystal structure. Fig. 1d presents the Transmission Electron Microscopy (TEM) image of $Ni(OH)_2$-Vi, which confirms the sheet-like morphology. HR-TEM image of $Ni(OH)_2$-Vi reveals distinct lattice fringes with an interplanar spacing of 0.232 nm, corresponding to the (015) planes of $Ni(OH)_2$ (Fig. 1e). Energy-dispersive spectroscopy (EDS) mapping of $Ni(OH)_2$-Vi demonstrates a homogenous distribution of V across the entire nanosheet, a feature not observed in $Ni(OH)_2$ (Fig. 1f; Fig. S3). X-ray photoelectron spectroscopy (XPS) was carried out to identify vanadate species on the $Ni(OH)_2$ surface and gain further insight into the changes in the electronic states of Ni and O induced by vanadate anchoring. Fig. 2a shows that V 2p spectra are composed of two main peaks located at 516.7 eV (V $2p_{3/2}$) and 524.4 eV (V $2p_{1/2}$), which correspond to VO_4^{3-}, confirming successful grafting of VO_4^{3-} onto the catalyst surface.[29] As shown in Fig. 2b, Ni 2p spectra of $Ni(OH)_2$-Vi present a markedly higher Ni^{3+} fraction (65.3 %) than that of $Ni(OH)_2$ (52.7 %). The concurrent decrease in peak intensity of the Ni 2p satellite further corroborates the promoted oxidation of Ni^{2+} to Ni^{3+}. It is attributed that surface reconstruction into NiOOH is accelerated by vanadate anchoring. Fig. 2c compares the O 1s spectra of $Ni(OH)_2$ and $Ni(OH)_2$-Vi. Each spectrum was deconvoluted into four components - chemisorbed oxygen ($O_{chemisorb}$) at 533.5 eV, hydroxyl oxygen species (O_{OH}) at 531.69 eV, oxygen vacancy (O_V) at 530.65 eV, and lattice oxygen (O_L) at 529.7 eV. $Ni(OH)_2$-Vi shows an increased O_V content (59.2 %) compared to $Ni(OH)_2$ (43.2 %), indicating that the activation process with vanadate promoted the formation of NiOOH containing a higher concentration of oxygen vacancies. Oxygen vacancies in MOOH can tune the local structure and electronic state of the catalyst, optimizing the adsorption energy of oxygen-generated reaction intermediates (OH*, O*, OOH*). Furthermore, the oxygen vacancies act as active sites, increasing the total number of active sites and increasing the catalytic activity.[30]

Electrochemical seawater oxidation performance

The electrochemical seawater oxidation properties of vanadate-anchored $Ni(OH)_2$ were tested under simulated alkaline seawater solution (1 M KOH + 0.5 M NaCl). Fig. 3a shows OER polarization curves of $Ni(OH)_2$ activated in 1 M KOH solution with various vanadate concentrations (0.25, 0.5, and 0.75 M). $Ni(OH)_2$-0.25Vi, which is activated with 0.25 M addition of vanadate, shows promoted OER activity compared to pristine $Ni(OH)_2$, indicating that the vanadate anchoring is effective for improving OER activity. Further increasing the vanadate concentration produced an additional enhancement in OER activity. The optimal concentration for OER activity was found at 0.5 M, above which the activity decreased with increasing concentration of vanadate. Fig. 3b summarizes the overpotential of vanadate-anchored $Ni(OH)_2$ for generating 10 mA cm^{-2} and 100 mA cm^{-2}. While pristine $Ni(OH)_2$ exhibits overpotentials of 328 mV at 10 mA cm^{-2} and 413 mV at 100 mA cm^{-2}, the optimized $Ni(OH)_2$-0.5Vi only requires 284 mV at 10 mA cm^{-2} and 346 mV at 100 mA cm^{-2}, confirming the superior OER activity of $Ni(OH)_2$-0.5Vi. Fig. 3c presents the Tafel slopes, where $Ni(OH)_2$-0.5Vi exhibits the lowest Tafel slope, further supporting its superior electrocatalytic OER kinetics.

DOI: 10.54227/mlab.20250006

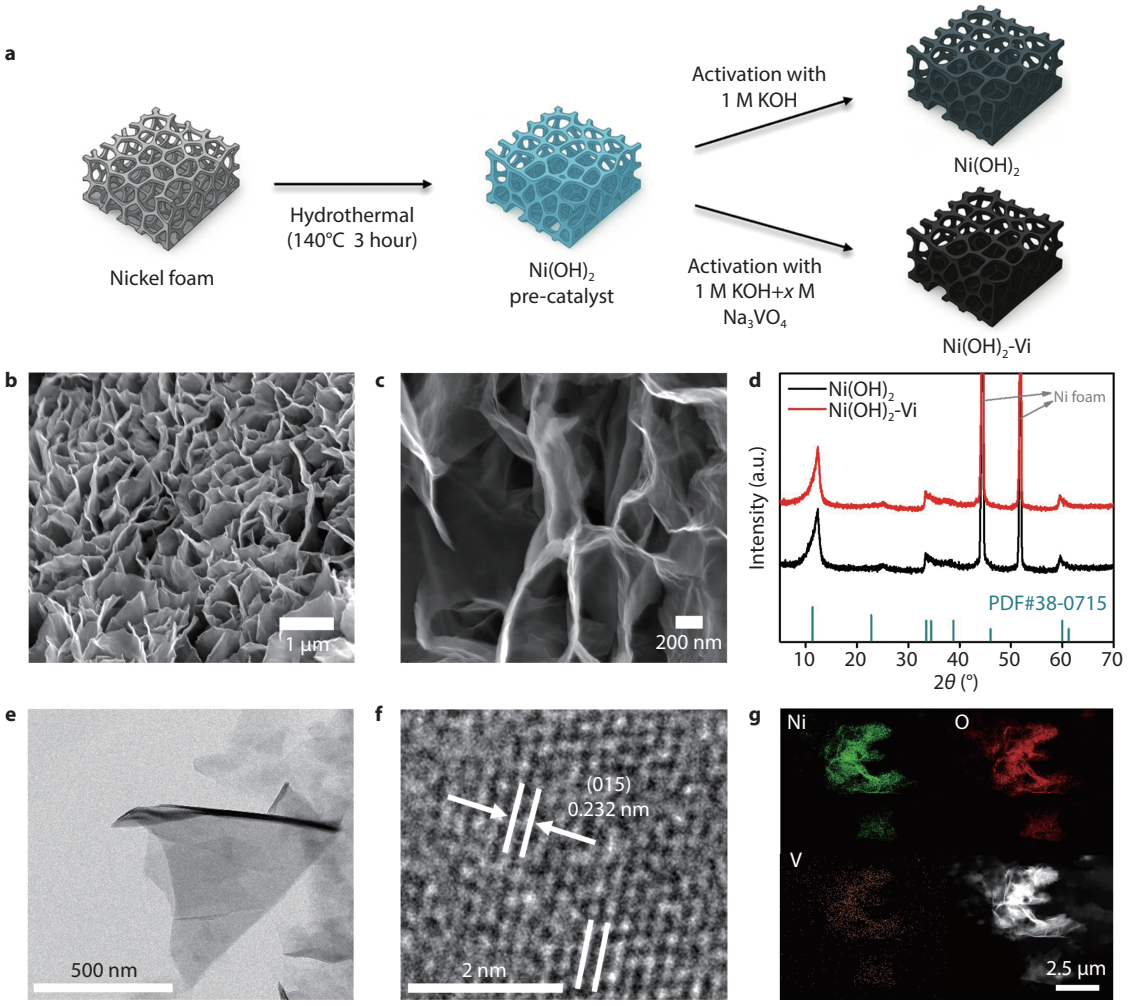

Fig. 1 Preparation and material characterizations of the $Ni(OH)_2$-Vi. **a** Schematic illustration of the preparation for $Ni(OH)_2$-Vi. **b**, **c** Scanning electron microscopy (SEM) images, **d** X-ray diffraction (XRD) patterns of $Ni(OH)_2$ and $Ni(OH)_2$-Vi. **e** Transmission electron microscopy (TEM) image of $Ni(OH)_2$-Vi. **f** High-resolution transmission electron microscopy (HR-TEM) image of $Ni(OH)_2$-Vi. **g** Energy-dispersive X-ray spectroscopy (EDS) elemental mapping of $Ni(OH)_2$-Vi.

To evaluate the influence of vanadate on the intrinsic activity of $Ni(OH)_2$, electrochemical surface area (ECSA) normalization was performed. ECSA was determined by the double-layer capacitance (C_{dl}) method, and cyclic voltammetry was conducted in the non-faradaic region (0.9 ~ 1.0 V_{RHE}) (Fig. S4). The C_{dl} and ECSA values of $Ni(OH)_2$, $Ni(OH)_2$-0.25Vi, $Ni(OH)_2$-0.5Vi, and $Ni(OH)_2$-0.75Vi are summarized in Fig. S5 and Table. S1. The ECSA values decrease as vanadate concentration in the electrolyte increases during the activation process. Normalization of the OER polarization curves by ECSA yielded trends consistent with those based on geometric area, confirming that $Ni(OH)_2$-0.5Vi exhibits the highest intrinsic activity among the evaluated electrocatalysts (Fig. 3d). To further substantiate the superior intrinsic activity of $Ni(OH)_2$-0.5Vi, turnover frequency (TOF) was investigated (Fig. 3e). The surface concentration of active sites per unit area was extracted from the linear dependence of the Ni^{2+}/Ni^{3+} oxidation peak current on scan rate (Fig. S6-7). On this basis, the turnover frequency (TOF) value of $Ni(OH)_2$-0.5Vi at 1.6 V_{RHE} was calculated to be 0.158 s^{-1} – 4.5 times higher than that of pristine $Ni(OH)_2$ (0.036 s^{-1}). Fig. 3f shows the electrochemical charge transfer resistance value (R_{ct}) that was investigated by Nyquist plot recorded on electrochemical impedance spectroscopy (EIS). $Ni(OH)_2$-Vi (~2.00 Ω) showed a value of R_{ct} that was obviously lower than that of the $Ni(OH)_2$ (~2.85 Ω), implying advantages of anchored vanadate species for facilitating charge transfer from the catalyst surface to the adsorbed chemical reactants (Table. S2).

To investigate the origin of the variation in seawater oxidation performance with varying vanadate concentrations in the electrolyte, XPS analysis was conducted on a series of $Ni(OH)_2$-xVi samples. As shown in Table. S3, the atomic ratio of Ni to V on the catalyst surface decreases with increasing vanadate concentration in the electrolyte, indicating enhanced vanadate coverage of the reconstructed phase. As the vanadate coverage increased, both the Ni^{3+} concentration and the density of oxygen vacancies (O_v) are increased (Fig. S8). These tailored electronic structures induce optimization of the adsorption energy for the reaction intermediates. To investigate the *OH adsorption strength, methanol probing experiments were performed (with 0.602 m L^{-1} methanol). Methanol, acting as a nucleophilic reagent, can readily react

DOI: 10.54227/mlab.20250006

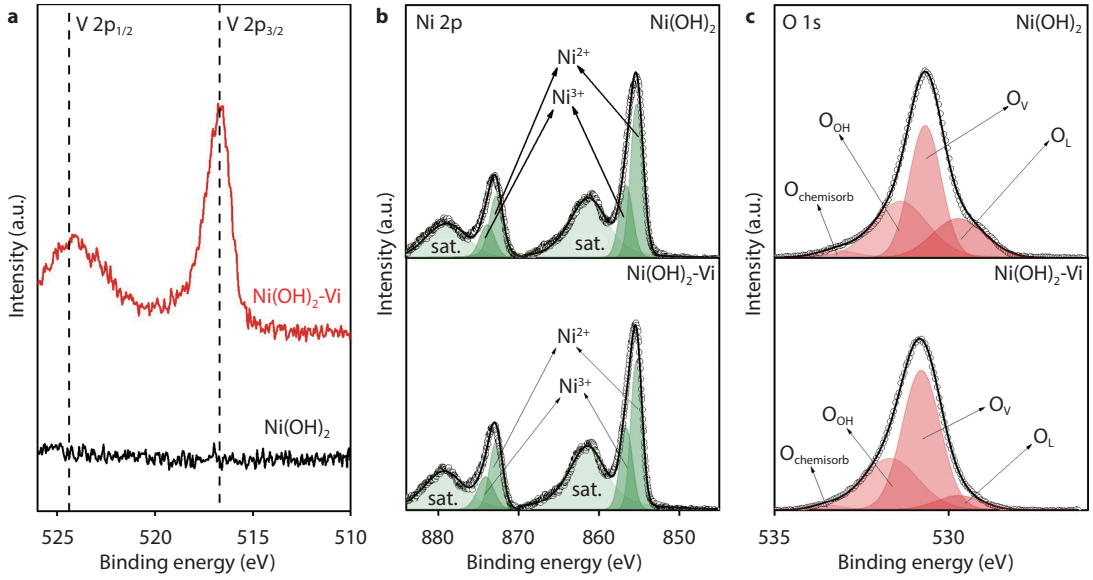

Fig. 2 X-ray photoelectron spectroscopy (XPS) spectra of the $Ni(OH)_2$ and $Ni(OH)_2$-Vi. **a** V 2p spectra of $Ni(OH)_2$ and $Ni(OH)_2$-Vi. **b** Ni 2p spectra of $Ni(OH)_2$ and $Ni(OH)_2$-Vi. **c** O 1s spectra of $Ni(OH)_2$ and $Ni(OH)_2$-Vi.

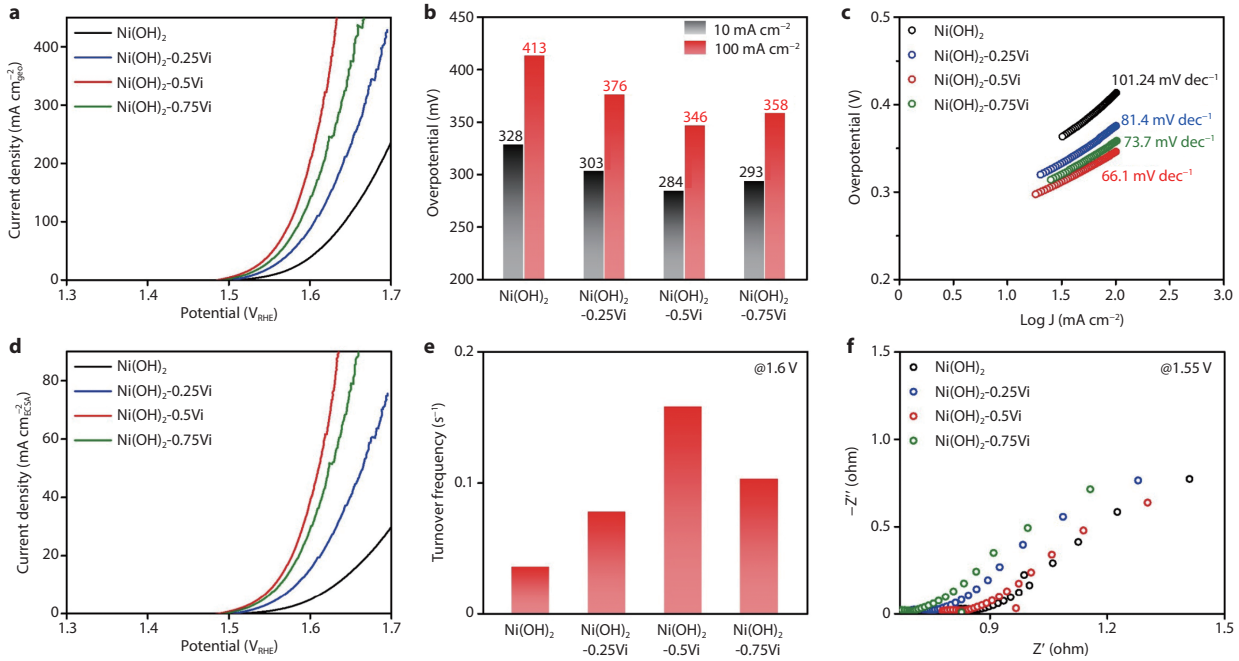

Fig. 3 Electrochemical seawater oxidation property of the $Ni(OH)_2$-xVi. **a** Polarization curves, **b** Corresponding overpotentials at 10 and 100 mA cm^{-2}, **c** Tafel plots. **d** Electrochemical surface area (ECSA) normalized polarization curves. **e** Turnover frequency of $Ni(OH)_2$-xVi. **f** Nyquist plot at 1.55V_{RHE} of $Ni(OH)_2$-xVi.

with electrophilic *OH intermediates generated during the OER process. This introduces a competitive pathway that interferes with the adsorption and accumulation of *OH species essential for OER progression. In Fig. S9, as vanadate coverage increases, the increase of current density is limited with addition of methanol, indicating that *OH is too strongly bonded to react with CH_3OH. These results show that the enhancement of OH adsorption energy on $Ni(OH)_2$ induces the enhancement of OER. However, too intensified *OH adsorption can hinder the subsequent formation of *O intermediates, ultimately impeding the OER kinetics.[31] This explains the reduced OER performance observed in $Ni(OH)_2$-0.75Vi, where excessive *OH binding becomes a limiting factor. In contrast, $Ni(OH)_2$-0.5Vi exhibits an optimal *OH adsorption energy, enabling balanced intermediate formation and thereby achieving the highest OER activity.

Mechanism study of vanadate anchoring-triggered OER activity enhancement

Electrocatalysts for OER undergo surface reconstruction under oxidizing conditions, forming the real active phase MOOH on the surface.[32–34] Because a facile reconstruction process

DOI: 10.54227/mlab.20250006

produces a larger population of highly active Ni^{3+} species, we first monitored the reconstruction behavior to elucidate the mechanism by which vanadate enhances OER activity. To electrochemically evaluate the surface reconstruction behavior, we tracked the activation of $Ni(OH)_2$ pre-catalyst in 1 M KOH with and without 0.5 M Na_3VO_4 by *operando* electrochemical impedance spectroscopy (EIS) over a range of applied potentials (Fig.3a-b). The characteristic peak observed in the high-frequency region (10^2 ~ 10^3 Hz) on Bode plots corresponds to oxidation of the metallic sites in the electrocatalyst. As the applied potential is increased, this peak progressively diminishes, and once the electrooxidation is complete, a new peak appears in the low-frequency region (~10^0 Hz) that arises from the uneven charge distribution characteristic of the OER process.[35] Fig. 4a depicts the activation process in 1 M KOH, and the electrooxidation peak persists throughout the scan and only at 1.6 V does it finally vanish. It indicates that the electrooxidation step is scarcely completed before the OER begins to develop. By contrast, activation in the vanadate containing electrolyte completed the electrooxidation step at 1.55 V, after which an OER associated peak emerged, indicating a more rapid surface reconstruction than that observed in plain 1 M KOH (Fig. 4b). This finding suggests that the simply adding vanadate to the electrolyte accelerates the formation of NiOOH, and it is in good agreement with the XPS results. *Operando* Nyquist plots were additionally investigated to assess the resistive components associated with electrooxidation and the OER (Fig. S10). The resistive elements obtained from the high-frequency semi-circle attributable to electrooxidation (R_1) and from the low-frequency semi-circle associated with the OER (R_2) were quantified and are visualized in Fig. 4c.[36] Consistent with the Bode plots, 1 M KOH activation exhibits only R_1 up to 1.6 V, after which an additional resistance component attributable to the OER appears. By contrast, vanadate-associated activation shows that the R_2 becomes detectable already at 1.55 V. Moreover, the magnitude of this OER resistance is markedly lower than 1 M KOH activation, indicating that the presence of vanadate in the electrolyte significantly enhances the intrinsic OER activity.

To elucidate the reaction mechanism of the catalysts after activation in the vanadate-containing electrolyte, we compared the OER activities of $Ni(OH)_2$ and $Ni(OH)_2$-Vi in 1 M TMAOH and in 1M KOH. Evaluating in 1 M KOH electrolyte for reference rather than containing 0.5 M NaCl was chosen to eliminate the kinetic hindrance arising from Cl^-. The bulky TMA^+ (Tetramethylammonium) cation interacts strongly with the negatively charged oxygen-containing intermediates ($*O_2^{2-}$ or $*O_2^-$) of the lattice-oxygen mechanism (LOM), substantially deteriorating the OER activity of catalysts that rely heavily on LOM pathway. Compared with the conventional adsorbate evolution mechanism (AEM), the LOM delivers superior OER performance because it bypasses the high-energy required *OOH intermediate formation step owing to the direct O-O coupling and thus breaks the thermodynamic scaling relationship that limits AEM-based catalysts.[37,38] Fig. 4d compares the polarization curves of $Ni(OH)_2$ and $Ni(OH)_2$-Vi measured in 1 M KOH and in 1 M TMAOH. $Ni(OH)_2$-Vi undergoes much more activity degradation in TMAOH than $Ni(OH)_2$. To quantify this activity degradation, we extracted the overpotential at the kinetically controlled low-current region and the Tafel slope (Fig. S11). For $Ni(OH)_2$, the differences in activity between KOH and TMAOH amount to 22 mV in overpotential at 10 mA cm^{-2} and 11.7 mV dec^{-1} in Tafel slope. In contrast,

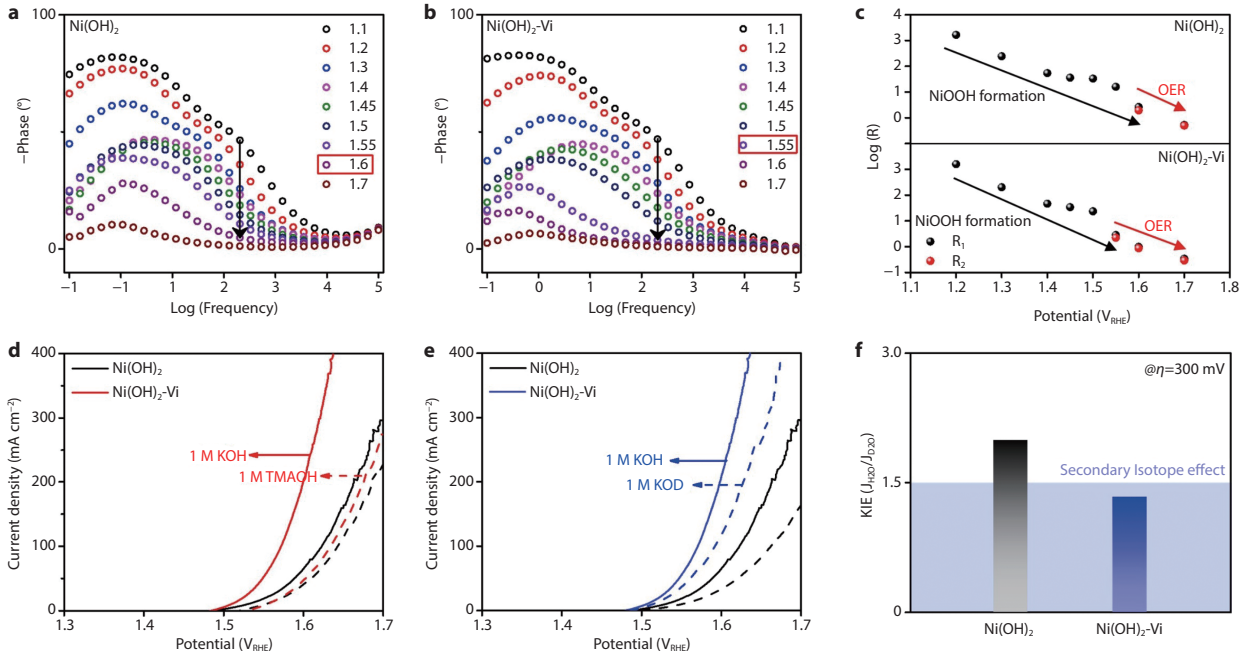

Fig. 4 Mechanism study of vanadate anchoring-triggered OER activity enhancement. **a**, **b** *Operando* bode plots during activation process of $Ni(OH)_2$ and $Ni(OH)_2$-Vi. **c** Correlation of the equivalent resistance and potentials fitted by Nyquist plot during activation process of $Ni(OH)_2$ and $Ni(OH)_2$-Vi. **d** Polarization curves measured with 1M KOH and 1M TMAOH of $Ni(OH)_2$ and $Ni(OH)_2$-Vi. **e** Polarization curves measured with 1M KOH and 1M KOD **f** The kinetic isotope effect of $Ni(OH)_2$ and $Ni(OH)_2$-Vi.

DOI: 10.54227/mlab.20250006

the corresponding variations are 46 mV and 23.16 mV dec^{-1} for $Ni(OH)_2$-Vi. The considerable variation in activity indicates that $Ni(OH)_2$-Vi strongly interacts with the TMA+ cation, relying more heavily on the LOM pathway.

The deprotonation step is widely recognized as the rate-determining step of LOM.[23,39] To investigate how vanadate anchoring influences the deprotonation step in LOM, we assessed the catalytic performance of $Ni(OH)_2$ and $Ni(OH)_2$-Vi in deuterated (1 M KOD, D_2O) and protonated (1 M KOH, H_2O) electrolytes. As shown in Fig. 4e, the performance of $Ni(OH)_2$ in 1M KOD/D_2O is significantly lower than that in 1M KOH/H_2O. This indicates that the deprotonation process significantly influences the overall kinetics of $Ni(OH)_2$, based on the fact that breaking an O-D bond requires much more energy than breaking an O-H bond. The kinetic isotope effect (KIE) value calculated at an overpotential of 300 mV for $Ni(OH)_2$ reaches 1.99 (Fig. 4f). This KIE value, greater than 1.5, indicates that the O-H bond cleavage step serves as a major rate-determining step in the overall kinetic mechanism, which is referred to as the primary isotope effect. In contrast, $Ni(OH)_2$-Vi exhibits a KIE value lower than 1.5, indicating that it is less affected by the sluggish kinetics of the deprotonation step at an overpotential 300 mV. This phenomenon, referred to as the secondary isotope effect, indicates that the deprotonation step is no longer the rate-determining step, thereby implying an accelerated LOM kinetics. Therefore, the vanadate anchored on the reconstructed catalytic surface acts as strong proton acceptors, further enhancing the overall OER activity.

Superiority of vanadate anchoring strategy in seawater oxidation

Given that surface anchoring of vanadate represents an unprecedented strategy for seawater oxidation, it was necessary to benchmark its seawater performance against electrocatalysts anchored with other oxyanions. For comparison, phosphate, the most commonly used oxyanion for chloride ion repulsion in seawater oxidation, was introduced following the same protocol used for $Ni(OH)_2$-Vi.[40–45] The $Ni(OH)_2$-Pi exhibits a sheet-like morphology and the same crystal structure as $Ni(OH)_2$ (Fig. S12-13). XPS analysis further confirms that phosphate is successfully anchored onto the reconstructed phase of $Ni(OH)_2$ (Fig. S14). The electrochemical activity of phosphate-anchored $Ni(OH)_2$ ($Ni(OH)_2$-Pi) was evaluated under simulated alkaline seawater. The OER polarization curves show that $Ni(OH)_2$-Pi requires substantially higher overpotentials than $Ni(OH)_2$-Vi across the entire current density range (Fig. 5a). The intrinsic activity of $Ni(OH)_2$-Pi was also evaluated by normalizing the OER polarization curves to its ECSA (Fig. 5b). After ECSA normalization, $Ni(OH)_2$-Pi showed an even larger performance gap relative to $Ni(OH)_2$-Vi owing to its higher ECSA value (Fig. S16). Consistent with the ECSA-normalized activity, $Ni(OH)_2$-Pi exhibits a significantly lower TOF than $Ni(OH)_2$-Vi, further highlighting the considerable enhancement in intrinsic activity achieved by the vanadate anchoring strategy (Fig. 5c; Fig. S17).

To explore the effect of vanadate anchoring on water oxidation under chloride-rich environments, we compared the polarization curves measured in 1 M KOH + 0.5 M NaCl (Brine) and 1 M KOH (Fresh water). As shown in Fig. 5d, $Ni(OH)_2$-Vi exhibits little difference between the LSV profiles recorded in the fresh and brine electrolytes, whereas $Ni(OH)_2$ and $Ni(OH)_2$-Pi show significant deviations under these conditions, indicating the superior chloride tolerance of $Ni(OH)_2$-Vi. To evaluate the extent to which chloride hinders the OER kinetics, Tafel slopes were also calculated based on the OER polarization curves in brine and fresh electrolytes (Fig. 5e). As shown in Fig. 5f, the seawater oxidation property at high current density and the seawater oxidation kinetics were evaluated based on Tafel slopes and the overpotential at 100 mA cm^{-2}. Pristine $Ni(OH)_2$ and $Ni(OH)_2$-Pi exhibit 20 mV and 16 mV increase in overpotential and 10.3 mV dec^{-1} and 9.3 mV dec^{-1} increase in Tafel slope when switching from fresh to brine electrolytes, indicating significant performance degradation under chloride-rich conditions. In contrast, $Ni(OH)_2$-Vi shows only a 5 mV increase in overpotential and a negligible 0.4 mV dec^{-1} change in Tafel slope, demonstrating both excellent seawater oxidation stability at high current densities and superior kinetic robustness against chloride-induced degradation compared to $Ni(OH)_2$ and $Ni(OH)_2$-Pi. It is attributed that vanadate anchoring can tailor the Cl^- adsorption energy on electrocatalyst surfaces through both electronic modulation and electrostatic repulsion, leading to a thermodynamically less favorable Cl^- adsorption energy while phosphate ion only acts as surface-adsorbed layers to repel Cl^- via electrostatic exclusion.

In contrast to simulated alkaline seawater, natural seawater presents a harsher environment for seawater oxidation, as catalyst degradation is driven by bromide in addition to chloride.[12] To evaluate the industrial applicability of the vanadate anchoring strategy, we carried out identical electrochemical tests in a 1 M KOH electrolyte prepared with natural seawater. Before testing, the seawater was rendered alkaline to induce the precipitation of $Mg(OH)_2$, $Ca(OH)_2$, and related species, which were subsequently removed by filtration as a pretreatment step. As illustrated in Fig. 5g, the polarization curves collected in natural seawater show a larger deviation from that of the fresh electrolyte than the deviation observed for the brine electrolyte. The Tafel slope and the overpotential at 100 mA cm^{-2} were determined from the polarization curves and compared with the corresponding values obtained in the fresh electrolyte (Fig. 5h-i). Compared with the fresh electrolyte, pristine $Ni(OH)_2$ required a 65 mV higher overpotential at 100 mA cm^{-2} in natural seawater electrolyte, and its Tafel slope increased markedly by 31.1 mV dec^{-1}. By contrast, $Ni(OH)_2$-Vi showed only a 22 mV increase in the overpotential at 100 mA cm^{-2} and a 13.4 mV dec^{-1} rise in the Tafel slope. The results from natural seawater highlight the viability of the vanadate-anchoring strategy for future industrial implementation.

To compare the long-term stability of oxyanion-anchored $Ni(OH)_2$, chronopotentiometry (CP) measurements were conducted at 100 mA cm^{-2} for $Ni(OH)_2$, $Ni(OH)_2$-Pi, and $Ni(OH)_2$-Vi. Fig. 6a displays the potential recorded for 200h in simulated alkaline seawater. The stability of the electrocatalyst was quantified by D_V, defined as the potential difference between the average values recorded during the first and last 5 % of the long-term stability test, normalized to 95 % of the total operation time.[46] Remarkably, $Ni(OH)_2$-Vi exhibits a D_V value of 0.198 mV h^{-1}, substantially lower than those of $Ni(OH)_2$

DOI: 10.54227/mlab.20250006

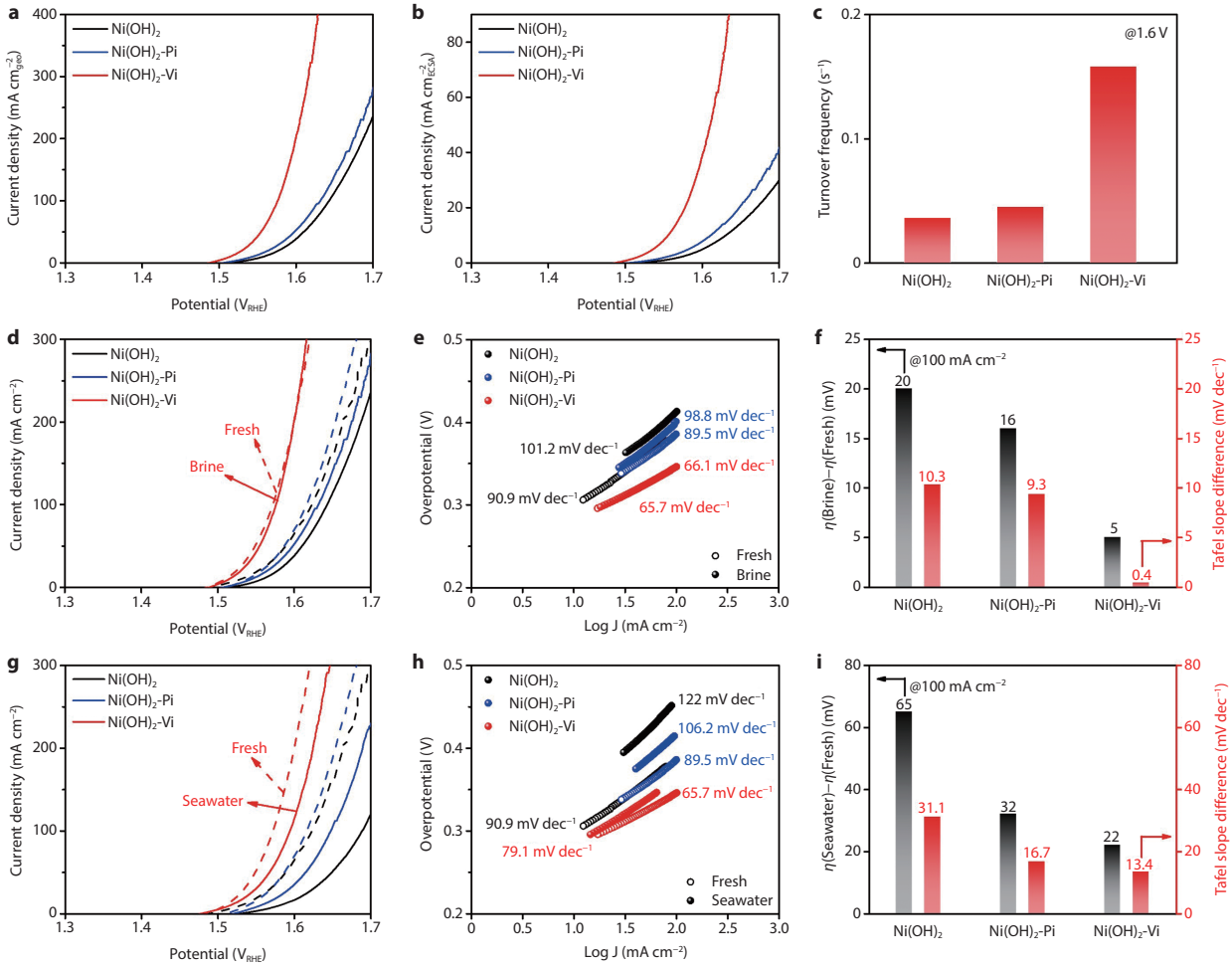

Fig. 5 Superior seawater oxidation property of vanadate anchoring strategy over phosphate anchoring strategy **a** Polarization curves comparing $Ni(OH)_2$-Vi and $Ni(OH)_2$-Pi. **b** Electrochemical surface area (ECSA) normalized polarization curves comparing $Ni(OH)_2$-Vi and $Ni(OH)_2$-Pi. **c** Turnover frequency comparing $Ni(OH)_2$-Vi and $Ni(OH)_2$-Pi. **d** Polarization curves measured with fresh electrolyte (1 M KOH) and brine electrolyte (1 M KOH + 0.5 M NaCl) and **e** corresponding Tafel plots. **f** Activity variation of overpotential and Tafel slopes under fresh electrolyte and brine electrolyte. **g** Polarization curves measured with fresh electrolyte and alkaline seawater (1 M KOH + seawater) and **h** corresponding Tafel plots. **i** Activity variation of overpotential and Tafel slopes under fresh electrolyte and alkaline seawater.

(0.812 mV h^{-1}) and $Ni(OH)_2$-Pi (0.780 mV h^{-1}). Moreover, whereas $Ni(OH)_2$ and $Ni(OH)_2$-Pi displayed pronounced potential fluctuations during prolonged operation, $Ni(OH)_2$-Vi maintained a steady potential for the entire stability test, underscoring its superior stability under seawater oxidation conditions.

To gain insight into the stability and structural evolution of $Ni(OH)_2$-Vi, post-operation analyses were conducted after 24 h of electrolysis at 100 mA cm^{-2}. Fig. 6c presents a post-operation SEM image, revealing that the $Ni(OH)_2$-Vi retains its sheet-like morphology even after prolonged electrolysis. Fig. 6d presents the post-OER Ni 2p XPS spectra of $Ni(OH)_2$-Vi, which shows the markedly higher Ni^{3+} fraction relative to the pre-operation $Ni(OH)_2$-Vi. It indicates an extensive reconstruction into NiOOH during continuous operation. Also, the O 1s spectra of $Ni(OH)_2$-Vi exhibit a pronounced increase in O_V component, indicating that continuous oxygen evolution through the LOM pathway has densely populated the electrocatalyst surface with oxygen vacancies (Fig. S18). Fig. 6e presents the post-OER HR-TEM image, revealing that a thick amorphous layer produced by surface reconstruction is clearly discernible on the sheet surface, matching the more amorphous XRD pattern observed after operation (Fig. S19). Also, the interior of the nanosheet still displays clear lattice fringes after long-term seawater electrolysis (Fig. S20).

Conclusion

We report a novel surface vanadate anchoring strategy that transforms ordinary $Ni(OH)_2$ into a chloride-tolerant, long-lived seawater-oxidation anode. This one-step electrochemical activation anchors vanadate onto the *in-situ* formed NiOOH layer. The surface anchored vanadate accelerates Ni^{2+} / Ni^{3+} conversion, steers the reaction toward a LOM pathway, and creates a persistent electrostatic barrier against Cl^- attack. Compared with the widely used phosphate anchoring, the vanadate approach affords markedly greater resistance to chloride-induced degradation and maintains stable operation in both simulated and real seawater electrolysis. These findings identify vanadate anchoring as a simple, scalable

DOI: 10.54227/mlab.20250006

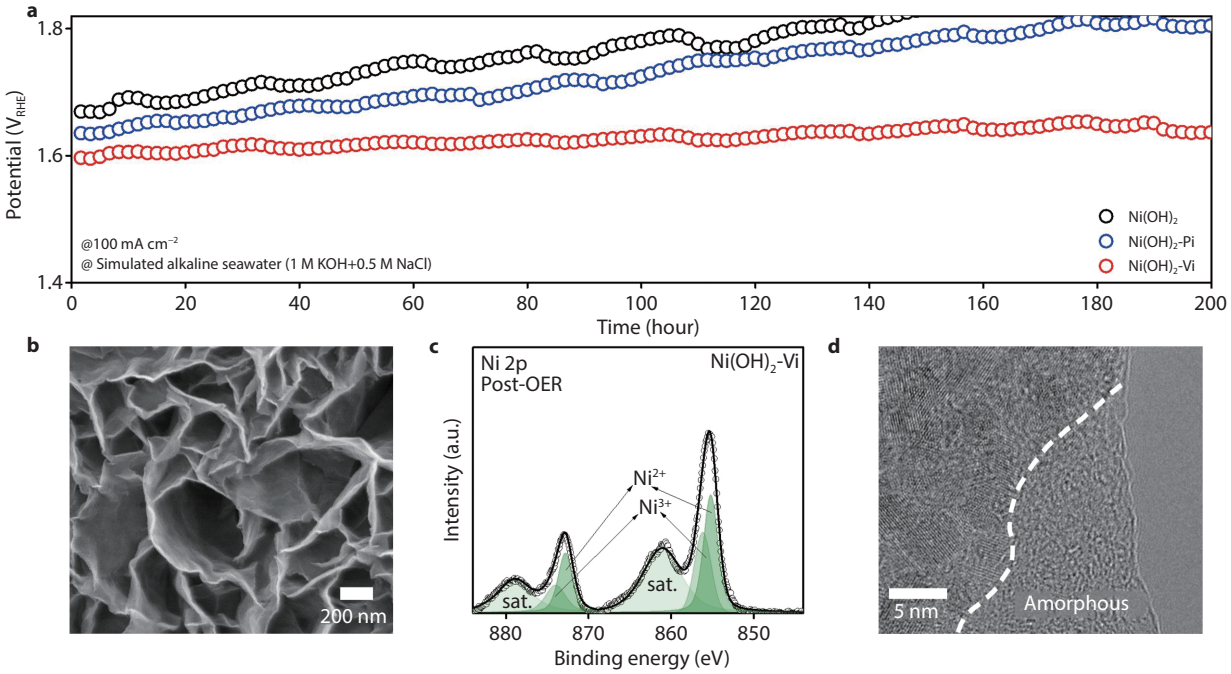

Fig. 6 Electrochemical stability in alkaline seawater and ex-situ characterization **a** Chronopotentiometry OER stability test at current density of 100 mA/cm^2 for 200 h under simulated alkaline seawater. **b** Post-OER SEM image of Ni(OH)$_2$-Vi. **c** Post-OER Ni 2p XPS spectra of Ni(OH)$_2$-Vi. **d** Post-OER HR-TEM image of Ni(OH)$_2$-Vi.

design principle for robust oxygen-evolving catalysts in seawater electrolysis.

■ CREDIT AUTHORSHIP CONTRIBUTION STATEMENT

Jooheon Sun: Writing – original draft, Conceptualization, Methodology, Investigation. **Jiseok Kwon**: Validation, Methodology. **Seunggun Choi**: Validation, Methodology. **Yeseung Lee**: Validation, Methodology. **Ungyu Paik**: Writing – review and editing, Supervision, Funding acquisition. **Taeseup Song**: Writing – review and editing, Supervision, Funding acquisition, Project administration.

■ DECLARATION OF COMPETING INTEREST

The authors declare that they have no known competing financial interests or personal relationships that could have appeared to influence the work reported in this paper

■ ACKNOWLEDGMENT

This work was supported by the National Research Foundation of Korea (NRF) grant funded by the Korea government [Ministry of Science and ICT (MSIT)] (2023R1A2C2004923).

■ REFERENCES

1. S. Zheng, K. Liu, Y. Li, B. Li, A. Usman, *Renew. Energy*, 2024, 227, 120465
2. J. A. Turner, *Science*, 2004, 305, 972
3. S. Evro, B. A. Oni, O. S. Tomomewo, *Int. J. Hydrog. Energy*, 2024, 78, 1449
4. M. S. Dresselhaus, I. Thomas, *Nature*, 2001, 414, 332
5. J. Kwon, H. Han, S. Choi, K. Park, S. Jo, U. Paik, T. Song, *ChemCatChem*, 2019, 11, 5898
6. J. Kwon, S. Sun, S. Choi, K. Lee, S. Jo, K. Park, Y. K. Kim, H. B. Park, H. Y. Park, J. H. Jang, *Adv. Mater.*, 2023, 35, 2300091
7. S. Choi, J. Kwon, C. Park, K. Park, H. B. Park, U. Paik, T. Song, *Energy & Fuels*, 2023, 37, 18128
8. S. Choi, J. Kwon, S. Jo, S. Kim, K. Park, S. Kim, H. Han, U. Paik, T. Song, *Appl. Catal. B*, 2021, 298, 120530
9. L. Ohlsson, *Phys. Chem. Earth, Part B*, 2000, 25, 213
10. T. Younos, *J. Contemp. Water Res. Educ.*, 2005, 132, 39
11. M. Khan, T. Al-Attas, S. Roy, M. M. Rahman, N. Ghaffour, V. Thangadurai, S. Larter, J. Hu, P. M. Ajayan, M. G. Kibria, *Energy Environ. Sci.* , 2021, 14, 4831
12. S. Zhang, Y. Wang, S. Li, Z. Wang, H. Chen, L. Yi, X. Chen, Q. Yang, W. Xu, A. Wang, *Nat. Commun.*, 2023, 14, 4822
13. P. Guo, D. Liu, R. Wu, *Small Struct.*, 2023, 4, 2300192
14. S. Zhang, W. Xu, H. Chen, Q. Yang, H. Liu, S. Bao, Z. Tian, E. Slavcheva, Z. Lu, *Adv. Mater.*, 2024, 36, 2311322
15. L. Yu, Q. Zhu, S. Song, B. McElhenny, D. Wang, C. Wu, Z. Qin, J. Bao, Y. Yu, S. Chen, *Nat. commun.*, 2019, 10, 5106
16. H. You, D. Wu, D. Si, M. Cao, F. Sun, H. Zhang, H. Wang, T. -F. Liu, R. Cao, *J. Am. Chem. Soc.*, 2022, 144, 9254
17. S. r. Dresp, F. Dionigi, M. Klingenhof, P. Strasser, *ACS Energy Lett.*, 2019, 4, 933
18. Z. Li, Y. Yao, S. Sun, J. Liang, S. Hong, H. Zhang, C. Yang, X. Zhang, Z. Cai, J. Li, *Angew. Chem. Int. Ed.*, 2024, 63, e202316522
19. X. Zhang, H. Zhang, Z. Chen, X. Chen, J. Wang, S. Wei, S. Liu, Z. Wang, F. Dai, M. Wang, *Adv. Funct. Mater.*, 2024, 1, 2418940
20. L. Shao, X. Han, L. Shi, T. Wang, Y. Zhang, Z. Jiang, Z. Yin, X. Zheng, J. Li, X. Han, *Adv. Energy Mater.*, 2024, 14, 2303261
21. Z. He, M. Ajmal, M. Zhang, X. Liu, Z. F. Huang, C. Shi, R. Gao, L. Pan, X. Zhang, J. J. Zou, *Adv. Sci.*, 2023, 10, 2304071
22. Y. Tang, C. Wu, Q. Zhang, H. Zhong, A. Zou, J. Li, Y. Ma, H. An, Z. Yu, S. Xi, *Angew. Chem. Int. Ed.*, 2023, 135, e202309107
23. H. Liao, G. Ni, P. Tan, K. Liu, X. Liu, H. Liu, K. Chen, X. Zheng, M.

DOI: 10.54227/mlab.20250006

Liu, J. Pan, *Adv. Mater.*, 2023, 35, 2300347
24. J. Kwon, H. Han, S. Jo, S. Choi, K. Y. Chung, G. Ali, K. Park, U. Paik, T. Song, *Adv. Energy Mater.*, 2021, 11, 2100624
25. T. Li, X. Zhao, M. G. Sendeku, X. Zhang, L. Xu, Z. Wang, S. Wang, X. Duan, H. Liu, W. Liu, *Chem. Eng. J.*, 2023, 460, 141413
26. A. K. Singh, S. Mukherjee, J. P. Singh, A. Gupta, P. Singh, *J. Power Sources*, 2025, 658, 238330
27. K. H. Shin, J. Park, S. K. Park, P. Nakhanivej, S. M. Hwang, Y. Kim, H. S. Park, *J. Ind. Eng. Chem.*, 2019, 72, 250
28. W. Shao, M. Xiao, C. Yang, M. Cheng, S. Cao, C. He, M. Zhou, T. Ma, C. Cheng, S. Li, *Small*, 2022, 18, 2105763
29. R. Kumar, T. Bhuvana, P. Rai, A. Sharma, *J. Electrochem. Soc.*, 2018, 165, B1
30. W. Yang, F. Qi, W. An, H. Yu, S. Liu, P. Ma, R. Chen, S. Liu, L. -L. Lou, K. Yu, *ACS Catal.*, 2024, 14, 5936
31. H. H. Kristoffersen, T. Vegge, H. A. Hansen, *Chem. Sci.*, 2018, 9, 6912
32. J. Chen, H. Chen, T. Yu, R. Li, Y. Wang, Z. Shao, S. Song, *Electrochem. Energy Rev.*, 2021, 4, 566
33. L. Gao, X. Cui, C. D. Sewell, J. Li, Z. Lin, *Chem. Soc. Rev.*, 2021, 50, 8428
34. Y. Zeng, M. Zhao, Z. Huang, W. Zhu, J. Zheng, Q. Jiang, Z. Wang, H. Liang, *Adv. Energy Mater.*, 2022, 12, 2201713
35. Z. Xu, M. Zhong, P. Liu, Z. Zhang, *J. Energy Chem.*, 2025, 106, 123
36. Y. Li, Y. Wu, M. Yuan, H. Hao, Z. Lv, L. Xu, B. Wei, *Appl. Catal. B*, 2022, 318, 121825
37. X. Wang, H. Zhong, S. Xi, W. S. V. Lee, J. Xue, *Adv. Mater.*, 2022, 34, 2107956
38. N. Zhang, Y. Chai, *Energy Environ. Sci.*, 2021, 14, 4647
39. H. Zhong, Q. Zhang, J. Yu, X. Zhang, C. Wu, H. An, Y. Ma, H. Wang, J. Zhang, Y. -W. Zhang, *Nat. Commun.*, 2023, 14, 7488
40. X. Gao, Y. Zhu, S. Yang, W. Zhang, R. Cao, *J. Energy Chem.*, 2025, 103, 393
41. J. Cai, D. Qu, X. He, P. Su, Q. Dong, Y. Li, B. Zhu, S. Yu, *Electrochim. Acta*, 2024, 507, 145067
42. C. Yang, Z. Cai, J. Liang, K. Dong, Z. Li, H. Sun, S. Sun, D. Zheng, H. Zhang, Y. Luo, *Nano Res.*, 2024, 17, 5786
43. M. Yu, J. Li, F. Liu, J. Liu, W. Xu, H. Hu, X. Chen, W. Wang, F. Cheng, *J. Energy Chem.*, 2022, 72, 361
44. H. Wang, N. Jiang, B. Huang, Q. Yu, L. Guan, *EES Catal.*, 2024, 2, 1092
45. C. Yang, C. Laberty-Robert, D. Batuk, G. Cibin, A. V. Chadwick, V. Pimenta, W. Yin, L. Zhang, J. -M. Tarascon, A. Grimaud, *J. Phys. Chem. Lett.*, 2017, 8, 3466
46. X. Kang, F. Yang, Z. Zhang, H. Liu, S. Ge, S. Hu, S. Li, Y. Luo, Q. Yu, Z. Liu, *Nat. Commun.*, 2023, 14, 3607